## **CONFERENCE PRE-PRINT**

# FIRST QUANTIFICATION OF VOLUME RECOMBINATION IN W7-X WITH EMC3-EIRENE

Y. FENG Max-Planck-Institut für Plasmaphysik Greifswald, Germany Email: feng @ipp.mpg.de

D. Reiter Heinrich-Heine-University Düsseldorf, Germany

H. Frerichs University of Wisconsin – Madison Wisconsin, USA

#### **Abstract**

The 3D boundary plasma transport code - EMC3-Eirene has recently been extended to treat volume molecule-assisted recombination (MAR). Using a typical detached plasma from W7-X as an example, we apply the latest EMC3-Eirene code version to perform a self-consistent analysis of the role of volume recombination processes, including MAR and electron-ion recombination (EIR) in the W7-X island divertor. Intrinsic carbon is assumed to be the only impurity species, and the radiation fraction  $f_{rad}$  is used as a control parameter. The simulation demonstrates that both EIR and MAR increase with  $f_{rad}$ , with the total volume recombination rate reaching approximately 30% of the total neutral source at  $f_{rad}$  =0.9. The MAR contribution is typically around a factor of three of that of the EIR when the radiation is located in the edge magnetic islands outside the last closed flux surface (LCFS). There are no noteworthy effects of volume recombination on detachment performance regarding the power load on the target, the neutral pressure in the divertor chamber, or the distribution of impurity radiation. Nevertheless, volume recombination significantly changes the relative population of atoms and molecules in front of the targets, which may be generally important for boundary plasma spectroscopy in fusion devices.

# 1. INTRODUCTION

Molecule-assisted recombination (MAR) processes are already active at plasma temperatures clearly above those required for the conventional electron-ion recombination (EIR) - a divertor plasma condition that is more readily attainable than that necessary for an intensive EIR. As a potential for the creation of a so-called gaseous divertor [1], MAR has attracted considerable attention in both tokamaks [2, 3] and linear devices [4, 5], and has been the subject of extensive research. In contrast, there has been a paucity of related studies in stellarators, especially in terms of modelling.

Unlike electron-ion recombination (EIR), which involves only charged particles, molecule-assisted recombination (MAR) processes [1] consist of a series of atomic reactions involving the participation of electrons, ions and molecules. In the present code version of EMC3-Eirene [6, 7], EIR is regarded as an external source for Eirene [8], while the MAR exit channel is treated as a cascading process, as are all other molecule fragmentation processes. Under certain conditions, this treatment of the MAR process can lead to an exponential growth of the neutral particle population (with extremely long or even infinite trajectories), which has unfavourable consequences for the coupled EMC3-Eirene system. This problem has recently been overcome by developing a new 'prediction-correction' method [9]. This enables the EMC3-Eirene code to treat volume recombination self-consistently, including both MAR and EIR.

The extended version of the EMC3-Eirene code now makes it possible, for the first time, to evaluate the role of volume recombination processes in helical devices. This paper will present a detailed analysis of the relevance and significance of EIR and MAR for the W7-X island divertor.

# 2. MOLECULE ASSISTED RECOMBINATION (MAR)

The MAR processes addressed in this work can be classified into two distinct reaction chains. In a hydrogen plasma, the first MAR chain begins with a process of charge exchange (CX, or aka 'conversion') between protons

and vibrationally excited hydrogen molecules:  $H_2(v) + H^+ \to H_2^+ + H$ . This process becomes resonant and even exothermal for vibrational levels at or above four. The formation of ion  $H_2^+$  is then followed by rapid dissociative recombination (DR):  $H_2^+ + e \to H + H$ . This second step is, at least, a two-step process in itself, because one of the product H atoms is initially formed in an electronically excited state  $H^*$ , which then, by further collisional or radiative transitions, can result in the final neutral H (ground state) atom, completing the MAR sequence. Through the entire chain of two-step (better: multi-step) processes, finally an electron and an ion  $H^+$  recombine to form an atom H and the molecule is dissociated into two H atoms. For convenience, henceforth in this paper the recombination process through the  $H_2^+$  ion channel will be referred to as 'CX-MAR' - a term derived from [5]. In addition to the dissociative recombination, there are other reactions that also participate in the breakdown of  $H_2^+$  ions. The most important are the processes of dissociative excitation  $H_2^+(v) + e \to e + H^+ + H$  and dissociative ionization  $H_2^+(v) + e \to 2e + 2H^+$ , which compete with the MAR sequence.

The second MAR chain under consideration is a combination of the processes of dissociative attachment (DA) and mutual neutralization (MN):  $H_2(v)+e \rightarrow H+H^-$  and  $H^-+H^+ \rightarrow H+H$ . Here again, in the second step initially one  $H^*$  is formed, which can then rapidly decay to H or, in a competing process channel, ionize to  $H^+$ . As in [5], this MAR sequence of processes through the  $H^-$  channel is designated as 'DA-MAR'. In addition to MN, there are again other reactions that eliminate the intermediate negative hydrogen ion. The two most relevant ones considered in this paper are  $H^-+H^+ \rightarrow H+H^++e$  and  $H^-+e \rightarrow H+2e$ , respectively.

If the intermediate  $H_2^+$  and  $H^-$  kinetic test particle ions are assumed to remain static until they are eliminated by further collisional processes, the two MAR reaction chains can both be combined into a compact single step form of  $H_2(v)+H^++e\to 3H$ . The corresponding volumetric recombination rates can be expressed as  $n_{H_2}n\langle\sigma v\rangle_{mar}^{cx}$  and  $n_{H_2}n\langle\sigma v\rangle_{mar}^{da}$ , respectively, where  $n_{H2}$  is the molecule density and  $n=n_e=n_i$ . The recombination rate coefficients  $\langle\sigma v\rangle_{mar}^{cx}$  and  $\langle\sigma v\rangle_{mar}^{da}$  are displayed in figure 1, compared with those of the processes of EIR and H-ionization from electron collisions. They are all given in the AMJUEL format [10] and are taken from published databases or CR-codes (loc.cit).

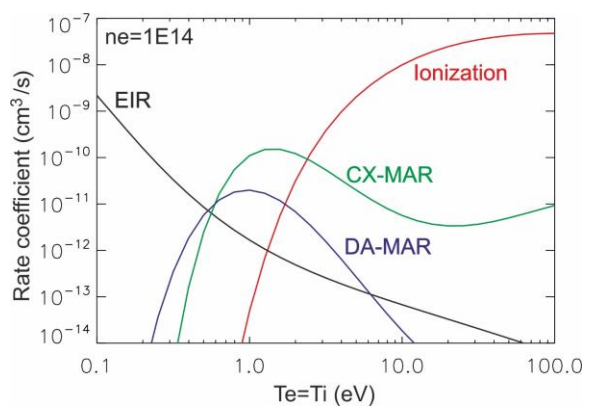


FIG.1. Rate coefficients of CX-MAR, DA-MAR, EIR and ionization of hydrogen atom at  $n=10^{14}$  cm<sup>-3</sup>, taken from AMJUEL database [10] (loc.cit). Note that they all depend on the plasma density.

## 3. QUANTIFICATION OF VOLUME RECOMBINATION IN W7-X

For a first evaluation of the role of volume recombination in the island divertor, we choose here a typical detachment discharge program from W7-X - #20180814.25. This discharge has been well studied both experimentally and numerically [11]. It was an ECR-heated hydrogen plasma with a port power of 5.5 MW. This discharge was operated with the so-called standard divertor configuration, bounded by the iota=5/5 island chain, which is the most-often studied magnetic configuration in terms of detachment. In the modelling, intrinsic carbon from the graphite target is assumed to be the only impurity species. Carbon atoms are sampled according to the flux deposition of the background ions on the graphite targets, accounting for chemical sputtering processes relevant for the detached plasmas of interest in this work. The total carbon yield is scaled by  $f_{rad}$  – the ratio between the impurity radiation and the total power into the computational domain, which is used as a control parameter and varied from 0.64 to 0.9. At the innermost boundary surface of the computation domain, situated approximately 8 cm inside the LCFS, the plasma density is co-varied with  $f_{rad}$  from 5 to 5.5×10<sup>13</sup> cm<sup>-3</sup>, in accordance with the experimental measurements. It is assumed that the anomalous diffusion coefficient,  $D=0.5 \text{ m}^2/\text{s}$ , applies to both hydrogen and carbon. The cross-field heat conductivity of electrons and ions is the same, with a value of 0.75 m<sup>2</sup>/s. The details of the simulation setup, processes and the primary numerical results for this discharge in the absence of volume recombination can be found in [11, 12]. With the new code version, we will clarify to what extent, in which aspects and under which conditions volume recombination can alter the island-divertor plasma.

In accordance with the preceding simulations not incorporating volume recombination, the present study, which includes volume recombination, continues to assume that there are no external particle sources, no pumps, and

that all PFCs, including the targets, have an ideal recycling coefficient of unity. In the presence of volume recombination, the total flux of the recycling neutrals,  $\Gamma_{recy}$ , can be expressed as

$$\Gamma_{recy} = \Gamma_{src} + \Gamma_{mar} + \Gamma_{eir}$$
 where  $\Gamma_{mar} = \Gamma_{mar}^{cx} + \Gamma_{mar}^{da}$ .

The terms on the right are, in order, the fluxes from the surface recombination on the target and the volume processes of CX-MAR, DA-MAR and EIR, respectively.

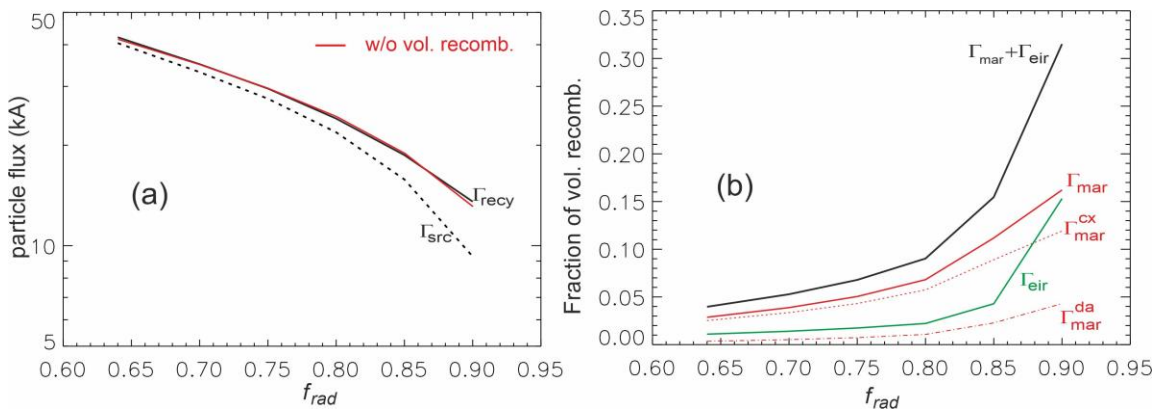


FIG. 2. (a) The total recycling flux (black solid) and the recycling flux from the targets (black dashed) in the presence of volume recombination as a function  $f_{rad}$ . The red solid curve is the total recycling flux in the absence of volume recombination. (b)  $f_{rad}$ -dependence of the fractions of contribution from different reaction processes.

Figure 2 depicts the results of the simulations, using  $f_{rad}$  as an independent parameter. The red solid curve in panel (a) on the left represents the total recycling flux in the absence of volume recombination, serving as a reference. In this instance,  $\Gamma_{recy} = \Gamma_{src}$ , meaning that all neutral particles are recycled from the target. Turning on the volume recombination processes results in an overall reduction in  $\Gamma_{src}$ , with the effect increasing at higher  $f_{rad}$  values, while the total recycling flux  $\Gamma_{recy}$  remains almost unchanged. In fact, our earlier work [11] already assumed that volume recombination should not significantly change the total recycling flux. In the high radiation range, the power balance is dominated by impurity radiation and hydrogen ionization, and the electron energy cost per ionization is almost a constant. Therefore, for a given  $f_{rad}$ , the total ionization source is determined by the remaining power, regardless of where the neutral particles are recycled (from surface or volume recombination). As will be shown later, the ionization cost actually increases slightly in the presence of volume recombination, but this small effect is compensated for by the heat flux to the targets.

The deviation between the black solid and dashed curve is the contribution of volume recombination, which is resolved in panel (b) on the right. As already indicated in Figure 2 (a), the total contribution of volume

recombination is relatively small. This is further elucidated by the black solid curve in Figure 2 (b), which represents the total contribution of volume recombination. It should be noted that all particle fluxes depicted in Figure 2 (b) are presented as a portion of the total flux  $\Gamma_{\rm recy}$ . At  $f_{rad}$  below 0.8, the total contribution of volume recombination is less than 10% of  $\Gamma_{\rm recy}$ . There is a rapid increase in the volume recombination contribution at  $f_{rad}$  >0.8, but it remains limited to approximately 30% even at  $f_{rad}$  =0.9. At this  $f_{rad}$  point, the majority of the radiation originates from closed field lines, as will be demonstrated later.

The CX-MAR process is primarily responsible for the reduction of  $\Gamma_{\text{src}}$ . Its contribution is approximately three times that of EIR, except at the highest radiation point,

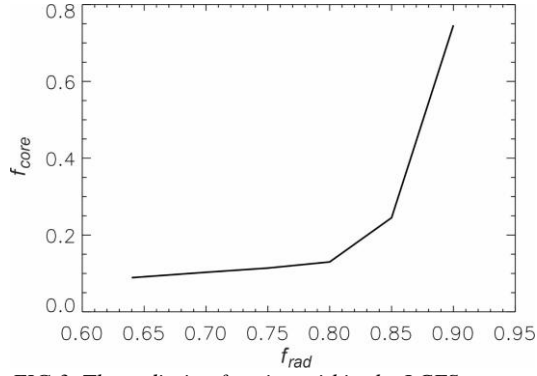


FIG.3. The radiation fraction within the LCFS increases rapidly at  $f_{rad}$ >0.8 and behaves similarly to  $\Gamma_{eir}$  (see figure 2 (b)).

where the latter slightly exceeds the former. In comparison, the contribution of DA-MAR can be considered minimal.

It would be interesting to ascertain whether the rapid increase in the total volume recombination rate at  $f_{rad}$  above 0.8 is a direct consequence of the increase in  $f_{rad}$  or it is a result of the associated radiation location. In this  $f_{rad}$  range, the 3D simulations also produce a rapid growth in the portion of radiation within the confining area, as displayed in Figure 3. The fraction of radiation inside the LCFS,  $f_{core}$ , increases significantly at  $f_{rad}$  values exceeding 0.8, as the radiation layer is entering the confinement region. The behaviour of  $f_{core}$  depicted in Figure 3 exhibits similarities to that of the total recombination rate illustrated in Figure 2 (b), especially to that of the electron-ion recombination (EIR). It appears that intense radiation on closed field lines facilitates the electron-ion recombination process. One of the most plausible reasons is that radiation condensation on closed field lines favours the build-up of plasma density due to the absence of a parallel particle transport channel. A comprehensive understanding of this point is the subject of ongoing research.

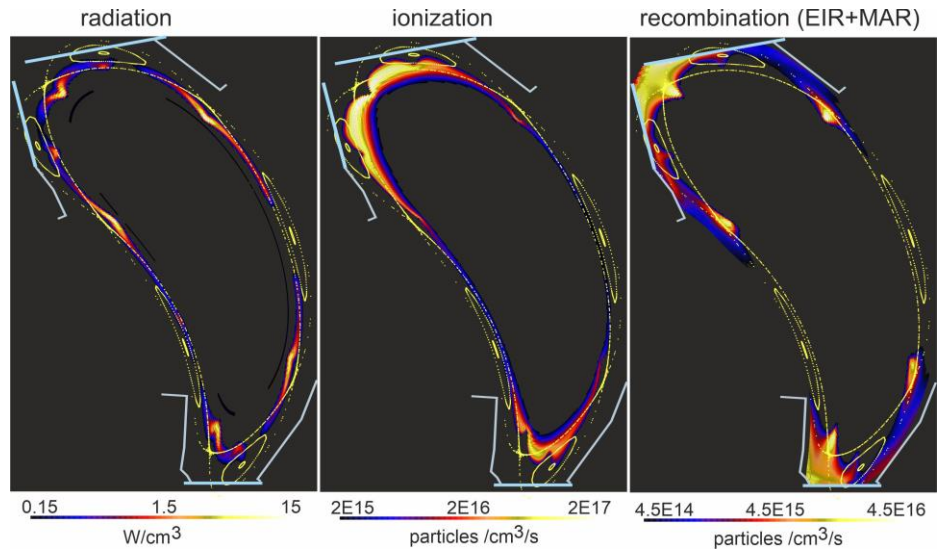


FIG.4. From left to right: distributions of carbon radiation, hydrogen ionization, and volume recombination at  $\phi$ =12 degrees. The three thick lines indicate three targets (two above and one below), while the thin lines indicate baffle plates. The Poincare plots illustrating the iota=5/5 island structure are generated from the vacuum field.

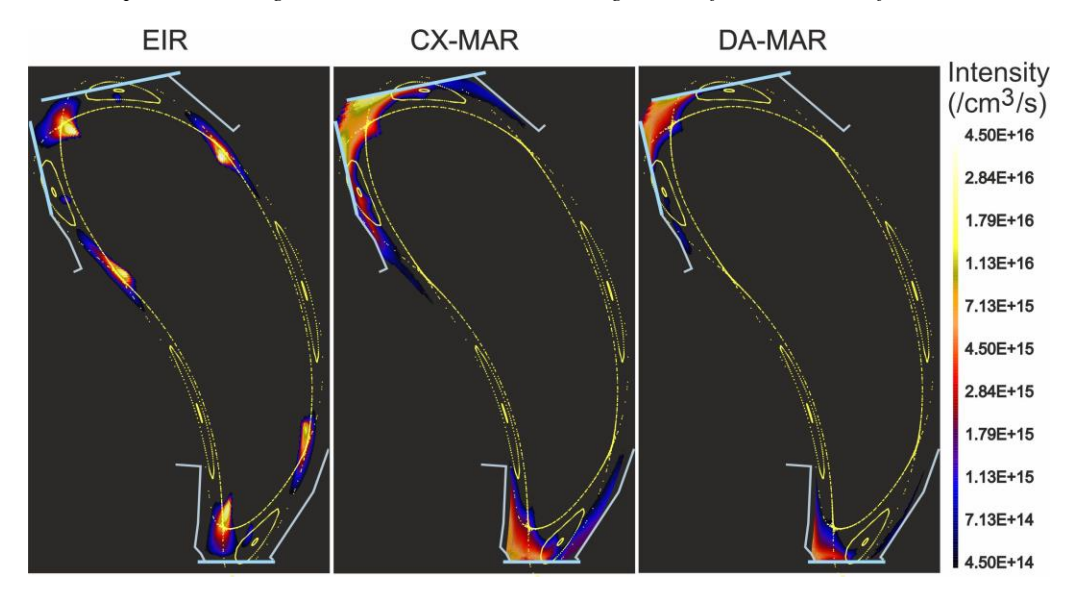


FIG.5. The location of various volume recombination processes in real space. The EIR is correlated with impurity radiation, whereas the MARs are controlled by molecule density.

Figure 4 depicts, from left to right, the distributions of carbon radiation, the total hydrogen ionization and volume recombination for the  $f_{rad}$ =0.9 case. The contour plots are presented at a toroidal position situated approximately at the centre of the strike line on the upper horizontal target. In the vicinity of this  $\phi$  location, plasma-surface

interaction occurs predominantly at the upper divertor, as evidenced by the ionization distribution in the middle panel of Figure 4. Due to the high radiation level, the radiation layer penetrates into the confinement area, exhibiting a radiation pattern that is closely correlated with the X-point geometry, known as X-point radiation (XPR) [13]. The magnetic islands at the edge are too cold for ionization, so it mainly occurs around the LCFS. The recycling neutrals are confined to the region further downstream between the targets and the ionization zone as a consequence of elastic plasma-neutral collisions.

The volume recombination (CX-MAR+DA-MAR+EIR) exhibits a distribution pattern that reflects both the radiation pattern and the distribution of recycling neutrals, more precisely the molecule density. For clarity, the various recombination processes are resolved and illustrated in Figure 5. The distributions of the various recombination processes can be explained with the help of Figure 6. The process of electron-ion recombination necessitates the presence of a dense and cold plasma that exists in the radiation zone, Figure 6. This is why there is a strong correlation between electron-ion recombination and carbon radiation. In contrast, the MAR processes require the participation of molecules that are located downstream in the vicinity of the target, as shown in Figure 6. The DA-MAR process takes place further downstream, as it requires lower temperatures than the CX-MAR process – Figure 1.

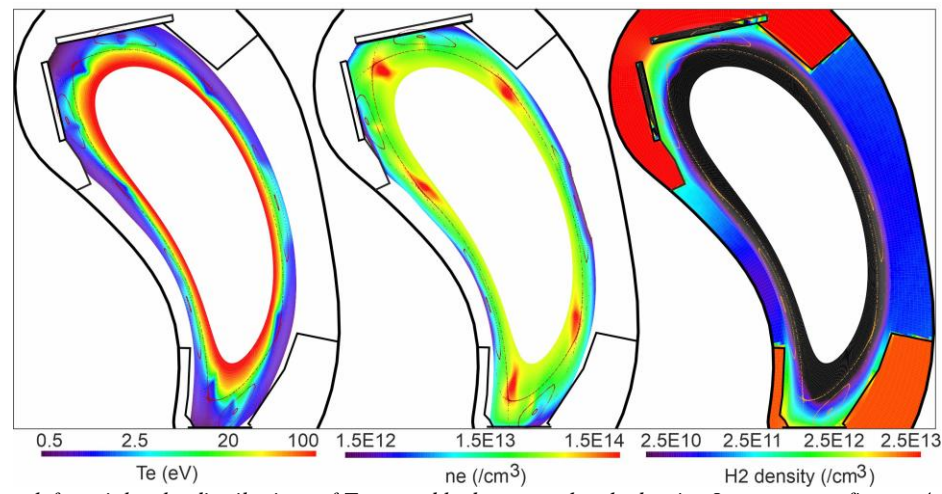


FIG. 6. From left to right: the distributions of  $T_e$ ,  $n_e$  and hydrogen molecule density. In contrast to figures 4 and 5, a different colour table is used here and more detailed structures of the in-vessel components are shown to highlight the molecule distribution.

The atoms generated from the MAR processes are effectively confined by the divertor arrangement. However, due to the limited plasma coverage of the local divertor, the majority of EIR-induced atoms are born outside the area where the divertor acts. Consequently, these atoms can contribute to enhanced wall recycling in the main

chamber, which, however, requires further investigation, particularly under conditions of higher heating power in the future.

The distributions of the various volume recombination processes in  $T_e$  space at  $f_{rad}$ =0.9 are displayed in Figure 7. The relative intensities, positions and distributions between the CX- and DA-MAR in  $T_e$  can be easily understood from their rate coefficients in Figure 1. In contrast, the behaviour of EIR is not to be expected from Figure 1. It takes place in the  $T_e$  range above those of the CX- and DA-MAR processes due to density effects. The plasma density in the radiation zone is much higher than in the near target region where the molecules are located, which overcompensates for the temperature effect. As a result, the EIR process takes place mainly in the vicinity

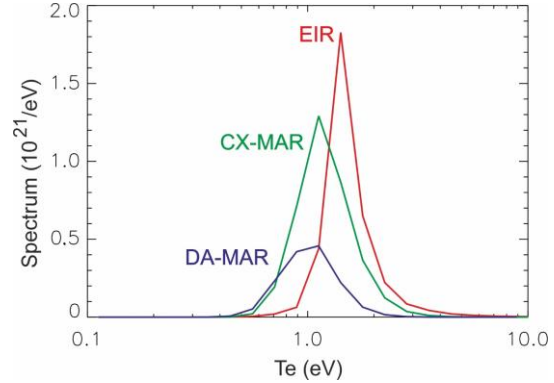


FIG.7. T<sub>e</sub>-spectrum of the EIR, CX- and DA-MAR processes for one of the ten identical divertor modules in W7-X.

of the radiation zone – figures 4 and 5, even though the electron temperature there is higher than in the region of the MAR processes.

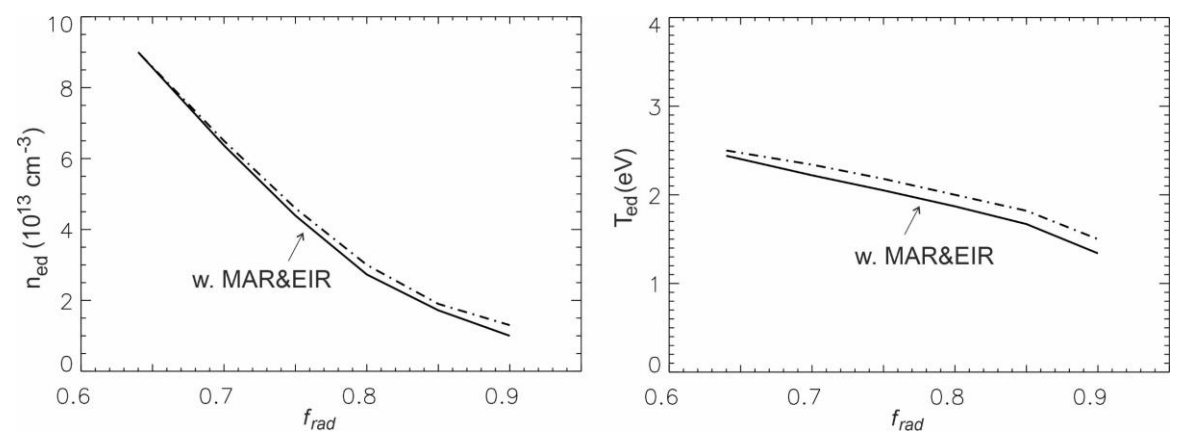


FIG.8. Comparison of  $f_{rad}$ -dependence of  $n_{ed}$  (left) and  $T_{ed}$  (right) between the cases with (solid) and without volume recombination (dot-dashed).

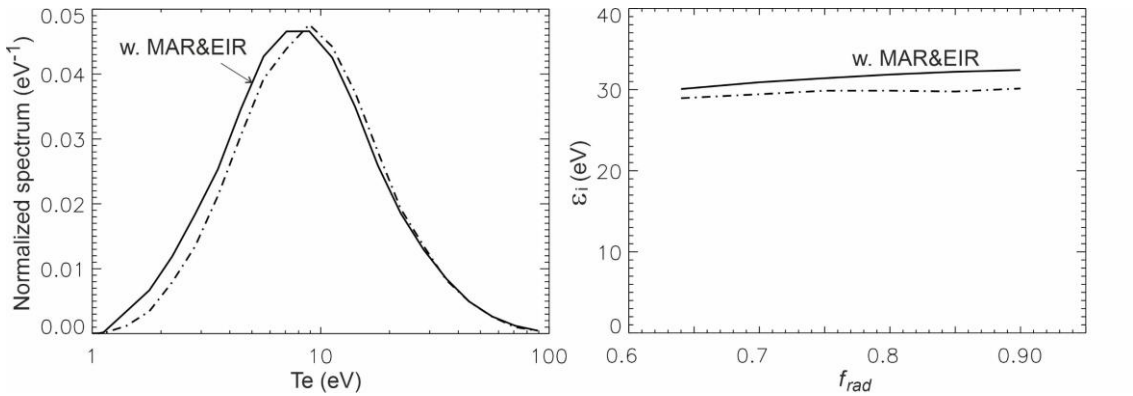


FIG. 9. Left:  $T_e$  spectrum of ionization source at  $f_{rad}$ =0.9 with (solid) and without (dot-dashed) volume recombination. The total ionization source is normalized to unity in both cases. Right: energy costs per ionization event as a function of  $f_{rad}$ .

Figure 8 compares the downstream plasma density  $n_{ed}$  and temperature  $T_{ed}$  between the two  $f_{rad}$  scans with and without volume recombination. They represent the respective average values in the last cells before the target, weighted by the thermal pressure of the plasma. Volume recombination provides a volume sink for the charged particles on the way to the target, reducing the plasma density at the targets, as shown on the left in Figure 8, especially in the high radiation range where volume recombination processes are more active. While the density effect can be explained intuitively, the reason why the volumetric particle processes lead to an overall decrease in  $T_{ed}$ , as shown on the right, is less transparent. To understand this point, we first examine the  $T_e$  spectrum of the ion source resulting from ionization and dissociation processes of the recycling neutrals. At  $f_{rad}$ =0.9, the  $T_e$  spectra of the ionization source with and without volume recombination are illustrated in Figure 9 on the left. In the presence of the volume recombination processes, the ionization source curve shifts to a lower  $T_e$  range. This is due to the fact that the dense and cold plasma where the volume recombination takes place has some confinement property for the resulting atoms. These atoms undergo a diffusion-like process as a result of charge-exchange with the background ions. The diffusivity of these atoms is proportional to the ratio of the ion temperature to ion density. The ionization of atoms at a lower temperature is more costly in terms of electron energy due to the increased probability of excitation relative to ionization. This is demonstrated in Figure 9 on the right. The increased ionization cost in the presence of volume recombination is the reason for the lower  $T_{ed}$  values shown in Figure 8.

With regard to the potential consequences of volume recombination on the performance of the island divertor, our principal concern is the peak heat load and the density of hydrogen molecules within the divertor chamber, which are depicted in Figure 10. There, the peak heat load is evaluated using the Lehmer method [14]  $q_{peak} = \iint q^p(s)ds/\iint q^{p-1}(s)ds$  with p=30, where q(s) represents the heat flux density over the entire surface s of all relevant targets. The molecule density shown in figure 10 represents the mean value across the in-divertor-

chamber cells. The dot-dashed lines are the results in the absence of volume recombination, which are used here as a basis for comparison.

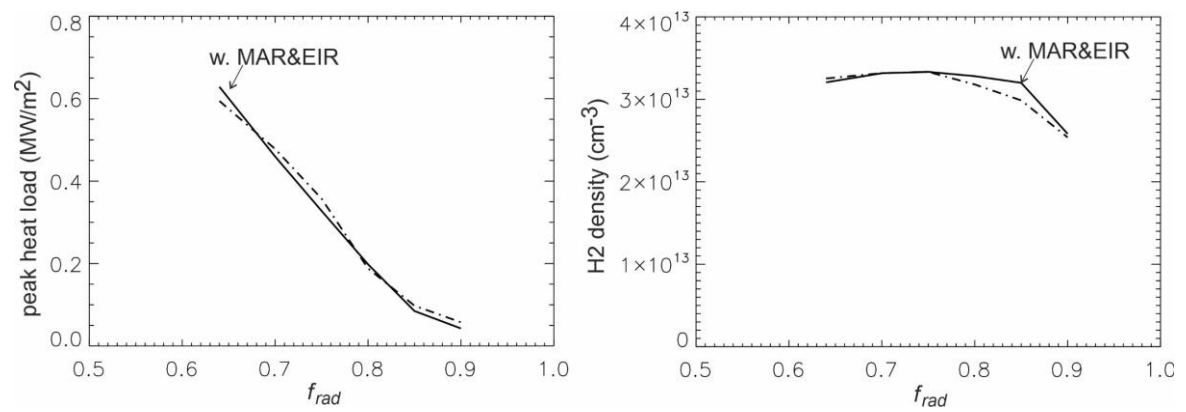


FIG.10. f<sub>rad</sub>-dependence of the peak heat load (left) and the hydrogen molecule density in the divertor chamber (right) in the cases with (solid) and without volume recombination (dot-dashed).

In comparison to figure 2, which shows a clear and systematic reduction in the integrated particle flux onto the targets in the presence of volume recombination, there is no significant alteration discernible in the peak heat load or divertor molecule density in figure 10. The reasons for this are complex and require further careful analysis. In the following, we provide some intuitive explanations, while leaving a more in-depth investigation for the future.

One of the most likely explanations for the small effect on the peak heat load is that volume recombination takes place mainly in the private flux region (PFR) and around the X-points radially in front of the PFR, whereas the peak heat load occurs on the O-point side of the magnetic island, away from the PFR (see figure 25 in [11]). The XPR pattern causes the plasma to condense near the X-point, reducing the heat flux into the PFR and creating a cold, dense plasma environment that favours the volume recombination processes. In the high radiation range investigated here, the residual heat is primarily transferred radially outwards by cross-field conduction through the radiation gaps between the radiating X-points [11] and finally reaches the targets along the field lines within the magnetic islands. The cross-field conduction paths are reflected in the temperature contour plots of figure 6 by the existing "warmer" plasma zones, which expand radially between the cold radiation zones. The topological separation between the volume recombination region and the remnant heat channel is thought to be the main cause of the weak effect of volume recombination on the peak heat load shown in figure 10.

The density of molecules in the divertor chamber is the result of a complex interplay between various factors, including the total neutral particle source, the source distribution and the transport of atoms and molecules. Under the high-radiation conditions of interest in this work, the total recycling flux is determined by the remaining power fraction available for ionizing the recycling neutrals, regardless of their origins. This explains why the total

recycling flux does not change very much after the volume recombination is activated. In terms of possible source location effects, the resulting volume-neutral source in the PFR ahead of the divertor gap should favour neutral compression in the divertor chamber. Nevertheless, this advantageous effect can be diminished by the wide distribution of the volume source (in part even beyond the divertor region). In the neartarget region, the transport dynamics of the neutrals are determined by charge exchange and elastic collisions, which result in a diffusion-like process. The diffusivity depends on the ratio of ion temperature and density, as well as the momentum transfer rate between ions and neutrals, in which atoms differ from molecules. In short, a comprehensive understanding of the potential consequences of volume recombination neutral compression necessitates

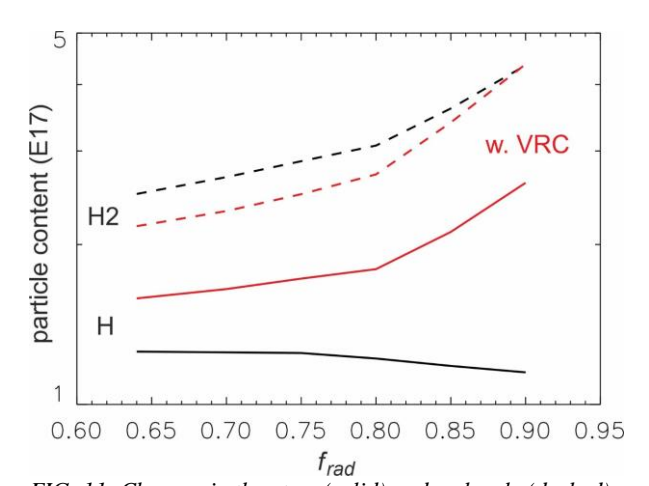


FIG. 11. Changes in the atom (solid) and molecule (dashed) population within the EMC3 domain as a function of  $f_{rad}$  in the cases with (red) and without (black) volume recombination.

decomposition of the relevant factors. However, this is challenging for the case under study, given the relatively minor role of volume recombination.

The most pronounced effects are observed in the relative population of atoms and molecules, as illustrated in figure 11. Shown are the developments of the atom and molecule contents within the plasma domain (the EMC3 simulation domain) as a function of  $f_{rad}$  for the two cases with and without volume recombination. In general, the MAR processes result in a reduction in the population of molecules and an increase in the population of atoms. In comparison, the EIR process produces only a source of atoms. The less pronounced impact observed in the molecular component can be attributed to the fact that PFCs typically act as a converter of atoms to molecules, which can partially offset the loss of molecules during the MAR processes. This hypothesis is supported by the co-variation of the two red curves depicted in figure 11 for the volume recombination case. The substantial alteration in the atom population may have significant implications for relevant diagnostics.

### 4. CONCLUSIONS

The EMC3-Eirene code has been extended to model molecule-assisted recombination, and was used for the first time on W7X to assess the effect of volume recombination on island divertor performance. A typical W7-X detachment discharge program was selected for the analysis. The simulation results show that both EIR and MAR increase with the radiation fraction  $f_{rad}$ . Nevertheless, the total contribution remains within approximately 30% of the total recycling neutral source even at  $f_{rad}$  =0.9. The volume recombination does not affect the total recycling flux; rather, it reduces the particle flux on to the targets. The MAR contribution is typically around a factor of three larger than that of the EIR when the radiation is located in the edge magnetic islands outside the last closed flux surface (LCFS). However, the two contributions become comparable as the zone of intensive radiation enters the confinement region during deep detachment, which is mainly attributed to a stronger increase in the contribution of EIR. No noteworthy effects on detachment performance are observed in terms of the peak heat load on the target or the neutral pressure in the divertor chamber. Nevertheless, the volume recombination processes markedly increase the concentration of atoms in the vicinity of the targets, while slightly decreasing the population of molecules. Clarification of the implications for relevant diagnostics, as well as a more in-depth analysis of the volume recombination processes under various experimental conditions, especially for different impurity species, will be the focus of future research.

# **ACKNOWLEDGEMENTS**

This work has been carried out within the framework of the EUROfusion Consortium, funded by the European Union via the Euratom Research and Training Programme (Grant Agreement No 101052200 — EUROfusion). Views and opinions expressed are however those of the author(s) only and do not necessarily reflect those of the European Union orthe European Commission. Neither the European Union nor the European Commission can be held responsible for them.

# REFERENCES

- [1] Janev R, Post D, Langer W, Evans K, Heifetz D and Weisheit J 1984 Journal of Nuclear Materials 121 10-16
- [2] Krasheninnikov S, Pigarov A and Sigmar D 1996 Physics Letters A 214 285–291 ISSN 0375-9601 URL https://www.sciencedirect.com/science/article/pii/0375960196001855
- [3] Kukushkin A, Krasheninnikov S, Pshenov A and Reiter D 2017 Nuclear Materials and Energy 12 984–988
- [4] Ohno N, Ezumi N, Takamura S, Krasheninnikov S and Pigarov A Y 1998 Physical Review Letters 81 818
- [5] Sakamoto M et al. 2017 Nuclear Materials and Energy 12 1004–1009
- [6] Feng Y et al. 2004 Contributions to Plasma Physics 44 57–69
- [7] Reiter D, Baelmans M and Boerner P 2005 Fusion Science and Technology 47 172-186
- [8] Frerichs H, Feng Y, Bonnin X, Pitts R, Reiter D and Schmitz O, 2021 Physics of Plasmas 28
- [9] Feng Y, Reiter D, Frerichs H, 2025 Nucl. Fusion 65 066008
- [10] Reiter D et al. 2000 Forschungszentrum Juelich GmbH 52425 URL https://eirene.de/Documentation/amjuel.pdf
- [11] Feng Y et al. 2021 Nucl. Fusion 61 086012
- [12] Feng Y et al. 2021 Nucl. Fusion 61 106018
- [13] Feng Y et al. 2024 Nucl. Fusion 64 086027
- [14] Lehmer D H 1971 Journal of Mathematical Analysis and Applications 36 183–200